applied sciences

MDPI

Article

Numerical Analysis of Pressure Drops in Single-Phase Flow Through Channels of Brazed Plate Heat Exchangers with Dimpled Corrugated Plates

Lorenzo Giunti [1,*], Francesco Giacomelli [2], Urban Močnik [3], Giacomo Villi [2], Adriano Milazzo [1] and Lorenzo Talluri [1,*]

1 Department of Industrial Engineering, University of Florence, Via di Santa Marta 3, 50139 Firenze, Italy; adriano.milazzo@unifi.it
2 Danfoss S.r.l., Via Corso Tazzoli 221, 10137 Torino, Italy; francesco.giacomelli@danfoss.com (F.G.); giacomo.villi@danfoss.com (G.V.)
3 Danfoss Trata d.o.o., Jožeta Jame 16, 1210 Ljubljana, Slovenia; urban.mocnik@danfoss.com
* Correspondence: lorenzo.giunti@unifi.it (L.G.); lorenzo.talluri@unifi.it (L.T.)

Abstract

The presented research examines the performance characteristics of Brazed Plate Heat Exchangers through computational fluid dynamics (CFD), focusing on pressure drop calculations for single-phase flow within full channels of plates featuring dimpled corrugation. This work aims to bridge gaps in the literature, particularly regarding the underexplored behavior near the ports for the studied technology and establishing a framework for future conjugate heat transfer studies. A methodology for the domain generation was developed, integrating a preliminary forming simulation to reproduce the complex plate geometry. Comprehensive sensitivity analyses were conducted to evaluate the influence of different parameters and identify the optimal settings for obtaining reliable results. The findings indicate that the $k - \varepsilon$ realizable turbulence model with enhanced wall treatment offers superior accuracy in predicting pressure drops, with errors within ±4.4%. Additionally, leveraging the information derived from CFD, a strategy to estimate contributions from different channel sections without a direct reliance on those simulations was developed, offering practical implications for plate design.

Keywords: heat exchanger; dimple pattern; CFD; pressure drops

Academic Editors: Hassane Naji and Alexander Mitov

Received: 10 July 2025
Revised: 25 July 2025
Accepted: 27 July 2025
Published: 29 July 2025

Citation: Giunti, L.; Giacomelli, F.; Močnik, U.; Villi, G.; Milazzo, A.; Talluri, L. Numerical Analysis of Pressure Drops in Single-Phase Flow Through Channels of Brazed Plate Heat Exchangers with Dimpled Corrugated Plates. *Appl. Sci.* **2025**, *15*, 8431. https://doi.org/10.3390/app15158431

1. Introduction

Heat exchangers are devices designed to allow the transfer of thermal energy between two or more fluids at different temperatures, without direct mixing between them. Various criteria can be considered to classify them [1]; when based on construction geometry, the acronym PHE (Plate Heat Exchanger) refers to a stack of metal plates with inlet and outlet ports, forming alternate channels through which substances flow. The primary feature of a PHE is the embossed pattern on the plate surfaces, which increases the heat exchange by promoting turbulence at low Reynolds numbers. The development of new corrugation designs, a passive enhancement technique, is the focus of extensive research [2,3], as it promotes energy savings, reduces industrial costs, and improves the efficiency of process equipment, contributing to environmental benefits, as demanded by the IEA [4].

The most common PHE is recognized [2] to be the herringbone (or chevron) type, consisting of a wavy surface with a characteristic β angle. In a manner similar to the scope of this study, computational fluid dynamics (CFD) simulations have been conducted to understand the flow patterns and improve the generalized heat transfer and pressure-drop correlations. It is well established that, as described by Sarraf et al. [5], two distinct structures, dependent on the Reynolds number *Re*, influence the mass transfer between the top and bottom grooves inside a herringbone channel: a helical motion, primarily aligned with the longitudinal direction, at low *Re*, and a cross-flow one, with the fluid following the corrugation until reaching the downstream end, at high *Re*.

In recent years, modifications to that design have been proposed to improve performance. Zhang et al. [6] analyzed a capsule-type PHE using CFD and compared it with chevron PHEs, demonstrating a higher Nusselt number Nu for *Re* below 3000, as well as a superior heat transfer performance index across all the examined *Re*; this was attributed to the presence of concave and convex surface features, which generate longitudinal and transverse vortices. Khail and Eris [7,8] introduced a PHE consisting of a basic unit constructed through a hyperbolic tangent function, finding an average Nu increase of 28% compared to herringbone PHEs and other new designs [7]. Additionally, they investigated the impact of various geometric parameters on flow characteristics [8]. Doo et al. [9] considered three novel plates with anti-phase, in-phase, and full-wave rectified secondary corrugations, achieving a more uniform distribution of the Nusselt number with respect to the traditional sinusoidal surface, with benefits in reducing thermal stress and transverse heat conduction. The same authors [10] also conducted a design of experiment to optimize the first of the geometries mentioned, explaining the impact of the secondary corrugation amplitude on the flow pattern and turbulence behavior. Gürel et al. [11] studied a PHE featuring a lung pattern that replicates a branching system with bronchial trees and bronchioles, supplied with water in a countercurrent configuration: they illustrated that this shape achieved effectiveness comparable to a reference chevron plate while providing 71.3% more heat transfer with fewer plates, leading to a reduction in cost.

In regard to alternative plate corrugations, a dimpled pattern, as shown in Figure 1, presents an undulated surface to enhance turbulence and create multiple contact points, thereby distributing pressure loads over a larger area. It is specifically employed for high-pressure applications, when the pack is assembled from plates that are brazed together in a vacuum oven to form a self-contained unit (BPHE), using brazing materials such as copper, stainless steel, or others, selected according to their compatibility with the operating fluid.

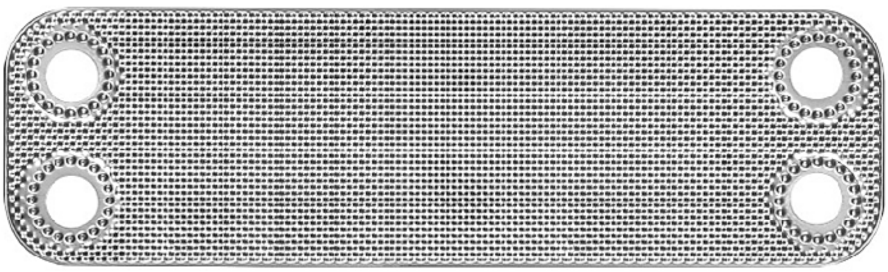

Figure 1. Heat plate featuring dimpled corrugation pattern [12].

The limited literature available on this type of design primarily focuses on the central portion of the heat plate (HP). Močnik et al. [13] performed an adiabatic CFD analysis of a sample created by replicating a small part of the channel which was derived from scanning measurements; they showed that the calculated pressure drops were matching the experimental data by employing the $k - \varepsilon$ turbulence model with enhanced wall treatment. Močnik et al. [14] performed flow visualizations on samples with a dimpled structure and pressure drop measurements, compared with numerical data, highlighting the absence of an evident, fully laminar regime even at Reynolds numbers below 230. Močnik and Muhič [15] carried out a series of experiments to evaluate the thermal performance of BHPEs with dimpled corrugation, in a counter-current configuration with two channels connected by a heat-conducting paste. From CFD results, they determined that the turbulent Reynolds Stress Model provided the most accurate description of heat transfer process, with the Nusselt number showing proportionality to $Re^{0.64}$.

A comparable flow pattern to that observed in BHPEs featuring a dimpled pattern is present in Pillow Plate devices (PPHEs), which are fabricated by spot-welding thin metal sheets together and subjecting them to hydroforming to achieve the desired inflation height. Indeed, the inner channel cross-section narrows to its minimum value in the vicinity of the welds, causing flow deflection and resulting in the formation of two distinct regions: the meandering core and the recirculation zone. Joybari et al. [16] conducted a comprehensive literature review on PPHEs, highlighting several key insights: notably, the flexibility of adjusting the outer channel depth, which offers the advantage of reducing the required heat transfer area compared to chevron PHEs, particularly in cases where flow rates on the two sides differ significantly. Kumar et al. [17] performed a Large Eddy Simulation of a periodic domain representing a PPHE channel supplied with water, considering both longitudinal and transverse types based on the respective pitch dimensions: they revealed differences in the vortex structures formed in the primary flow for the two cases, as well as the Nusselt number distribution, which reaches its maximum at the stagnation point in front of the welding spots for the longitudinal arrangement. Norouzi et al. [18] carried out CFD analyses to investigate the influence of various geometric parameters on local entropy generation in a PPHE, finding that it rises with channel height and the adoption of a transverse configuration, while the diameter of the spot weld has a negligible effect. To estimate the Nusselt number in PPHEs, Piper et al. [19] developed a two-zone model based on the characteristic flow pattern, as previously described, demonstrating an accuracy within ±15% when compared to CFD results, under conditions of fully turbulent and a thermally developed boundary layer. Later, Piper et al. [20] numerically examined the effect of dimpled surfaces on a PPHE, showing a 2.2% improvement in the heat transfer coefficient, attributed to the continuous disturbances induced in the turbulent boundary layer, which enhanced mixing; additionally, the slightly larger cross-sectional area led to a reduction in pressure losses, resulting in an 11.2% increase in thermo-hydraulic efficiency.

All the cited references pertain to single-channel simulations with a fixed wall temperature, which limits the full understanding of the actual thermal interaction between the inner and outer passages. To the best of the author's knowledge, only the study by Zibart and Kenig [21] focused on conjugate heat transfer calculations for a PPHE operating in a counter current-flow arrangement. Their findings revealed that assuming one-dimensional heat conduction to approximate the plate thermal resistance, in cases of high material conductivity, led to deviations exceeding 50%; this error could be mitigated by introducing a fit function that accounts for the three-dimensional nature of heat transfer.

Currently, there is a gap in the performance analysis of entire channels in relation to the studied technology, as previous research has primarily focused on the central section, overlooking the behavior near the ports. This work provides a comprehensive CFD analysis of turbulent single-phase flows within channels formed by two heat plates with a rounded-dimple corrugation pattern, aiming to validate a workflow that can serve as a basis for evaluating pressure drop and conducting future conjugate heat transfer simulations. The results extend the analysis to a full channel and a range of objects with varying dimensions, thereby enhancing the understanding of the flow field and deriving a more robust methodology for general investigations. Additionally, a strategy was developed to estimate the pressure drop contributions from different sections of the channel, providing a useful tool that does not rely on CFD simulations.

2. Methodology

2.1. Geometry Generation

The primary difficulty in preparing the computational domain examined for CFD calculations lies in accurately constructing the channels defined by the complex surface of the HP and the brazed areas.

While the central region of the channel, as shown in Figure 2, is composed of interconnected base unit volumes—highlighted in red in Figure 2c—and could be approximated by distributing a double cosine wave across space, predicting the outer zones near the ports remains challenging due to the variations in dimple shape and size. Indeed, they not only differ from those in the middle part but also vary across geometries to meet certain application requirements.

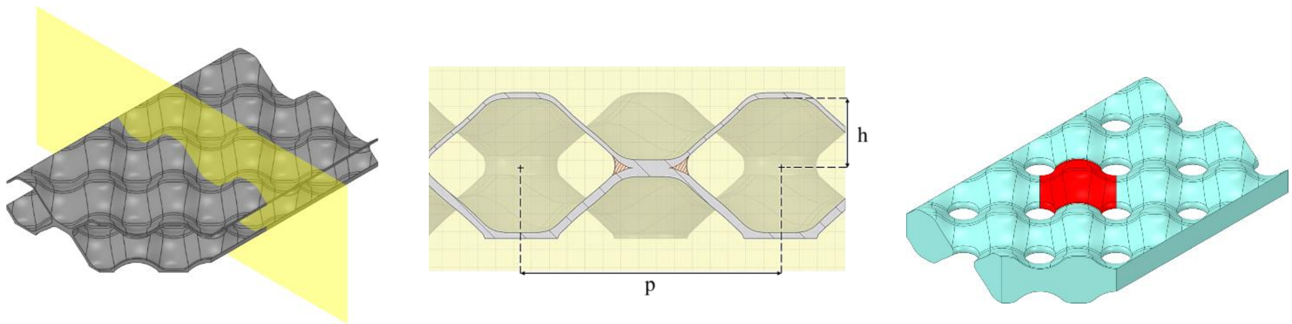

(**a**) (**b**) (**c**)

Figure 2. Details of the central region of (**a**) a two-plate assembly with dimpled corrugation; (**b**) cross-sectional view illustrating the characteristic geometrical parameters; (**c**) corresponding flow channel.

For a realistic representation of the corrugated component, the HP surface has been obtained implementing forming simulations in the commercial tool Ansys Forming 23 R1, employing the theory of explicit dynamics [22] when handling large deformations and strains, along with complex contacts. The process involves a time-discretized analysis, where the sheet metal plate, made of steel grade AISI 316L, is treated as a surface with zero physical thickness, which was assigned mathematically. The material behavior was specified by modeling the yield surface based on the work of Barlat et al. [23], with the flow stress derived from the combination of uniaxial tension and bulge tests. The input objects were the CAD models of the pressing dies, including the waffles and the forming ring. The procedure was validated by comparing the resulting HPs with 3D scanning measurements of plates that were actually produced. Three distinct geometries, differing in overall size and dimple features, were generated based on a series of tests conducted on their corresponding channels, as detailed in the following sections. An example of the simulated HPs is presented in Figure 3a.

In examining the repetitive pattern, the primary parameters defining the heat plate, as indicated in Figure 2b, are the profile height h, which determines the channel height, and the longitudinal and transverse pitch, denoted by p (equal in these cases). The overall dimensions, as shown in Figure 3b, are specified by the width W, length L, the diameter D_p of the ports, and their distance L_p. The values for the three HPs, scaled relative to those of the third one, are summarized in Table 1.

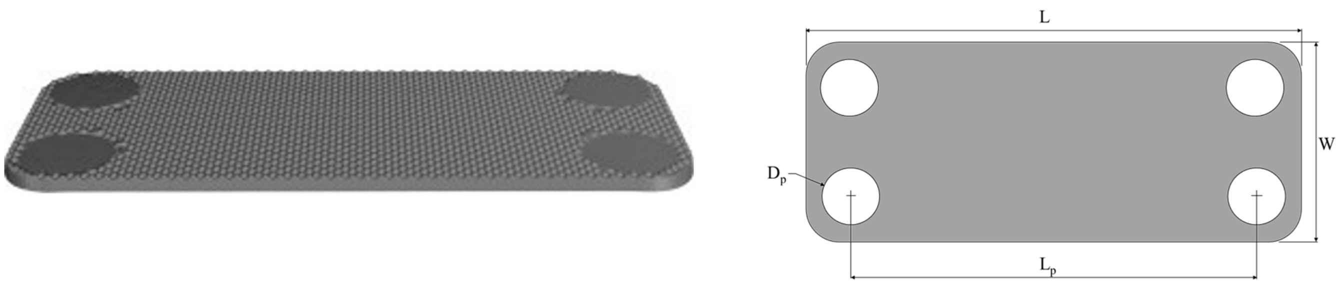

(**a**) (**b**)

Figure 3. Heat plate surface: (**a**) resultant geometry from the forming simulation; (**b**) schematic representation of its overall dimensions.

Table 1. List of investigated plate geometries.

Sample	h/h^*	p/p^*	W/W^*	L/L^*	D_p/D_p^*	L_p/L_p^*
S1	1.11	1.21	1.25	0.58	1.78	0.53
S2	0.74	0.92	1	0.65	1	0.61
S3	1	1	1	1	1	1

The computational domain was generated by first converting the STL file from the forming simulation into a CAD model using surface patches, thereby replicating the initially imported HP. This approach was adopted as it offers the advantage of enabling conformal meshes, which are beneficial for future conjugate heat transfer (CHT) simulations. The comparison between the converted and original HP models has shown a maximum deviation of 1.5% of the h.

Conversely, due to the method used to construct the domain, the size of the derived CAD file and the corresponding grid are not compatible with modeling an entire PHE, which typically consists of dozens to hundreds of plates.

2.2. Theoretical Background and Modeling

In examining the whole pressure drops across a PHE device, three main components [24] can be identified, namely: those occurring in the inlet and outlet manifolds and ports, within the HP passages, and due to elevation changes. Although the pressure loss term associated with the manifolds can be calculated by using an empirical equation [24], its uncertainty significantly impacts the performance evaluation, particularly at high mass flow rates.

Because of the mentioned limitations in pre-processing preventing the estimation of that contribution and in pursuit of a well-established procedure, the analysis has been focused on single channels supplied with water at ambient temperature, tested in the same rig as described by Močnik et al. [13]. The present activity extends that study, which considered only the central portion of the HP (referred to as the matrix), by investigating both complete and partial HPs.

A scheme of the system is depicted in Figure 4a.

In summary, the test bench consists of two large stainless-steel vessels to maintain uniform pressure conditions at both ends of the sample—highlighted in red in Figure 4a—which is clamped between them. Detailed information about the test rig is provided in [13].

To replicate the setup, a CAD model of only the fluid domain, comprising the volumes and the channel, was created, as shown in Figure 5. The geometry was modeled using SpaceClaim, part of the Ansys software suite 22 R2.

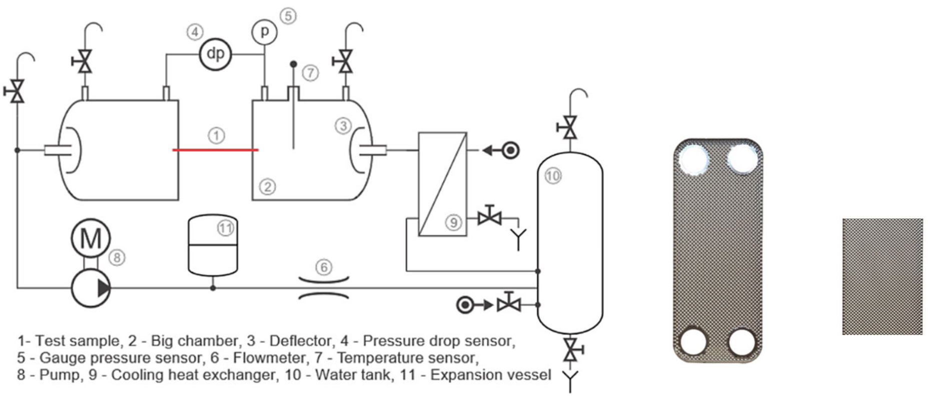

(**a**) (**b**) (**c**)

Figure 4. Test bench: (**a**) schematic; (**b**) full heat plate; (**c**) matrix obtained from central-portion cut.

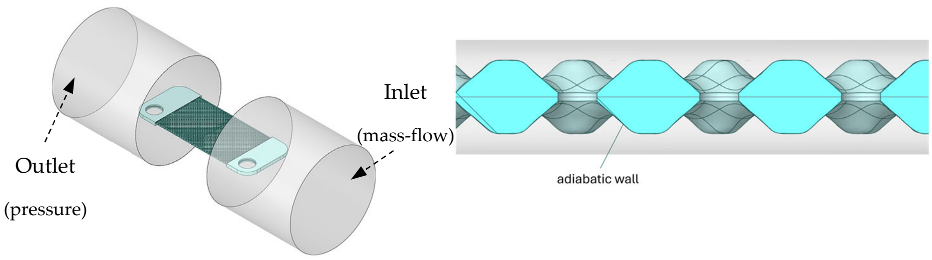

(**a**) (**b**)

Figure 5. Fluid domain: (**a**) the dimpled corrugated channel (light blue) along with the inlet and outlet vessels (gray); (**b**) cross-sectional view highlighting the channel volume details.

The editing of the HP includes adding the brazed joints, which appear as copper material bridges, connecting contact points between the assembled plates, along with the walls around the closed ports that prevent fluid entry on that side. The brazed material is highlighted in orange in Figure 2b.

To simplify their complex shapes, especially when blending with the HP surface without discontinuities, they were approximated as cylinders between the dimples, in the middle part; the diameters were assigned based on the averaged values resulting from optical measurements.

The working fluid, water, is modeled as incompressible and single-phase, with constant properties imposed by knowing the operating temperature and pressure.

The following equations govern the fluid dynamics problem under investigation:

$$\frac{\partial \rho}{\partial t} + \nabla \cdot \left(\rho \vec{u} \right) = S_m, \tag{1}$$

$$\frac{\partial \left(\rho \vec{u} \right)}{\partial t} + \nabla \cdot \left(\rho \vec{u} \vec{u} \right) = -\nabla p + \nabla \cdot \left(\overline{\overline{\tau}} \right) + \rho \vec{g} + \vec{F}. \tag{2}$$

representing the laws of conservation of mass (1) and momentum (2), where $\vec{u}$ is the velocity vector; S_m is a general mass source term; p is the pressure; and $\vec{F}$ denotes the resultant body force. In the present study, $S_m = 0$, $\vec{F} = 0$, and adiabatic wall conditions were assumed, with no heat transfer to the surroundings. Under these assumptions, Equations (1) and (2) form a decoupled system, with $\rho = const$.

Steady-state analyses were performed using the commercial software Ansys Fluent 22 R2 [25].

The stress tensor term $\overline{\overline{\tau}}$ has been computed with a two-equation turbulence model. Mocnik et al. [13] reported the existence of a channel entrance region of unknown length, where the flow is not fully turbulent. Nevertheless, the Reynolds numbers inspected consistently exceeded 200, which is a threshold commonly applied [5,26] for turbulence modeling in CFD simulations of BPHEs.

Both $k-\varepsilon$ and $k-\omega$ schemes were initially tested to determine the most suitable option for the studied BPHEs. For the former, the realizable variant with enhanced wall treatment (EWT) was chosen due to its ability of capturing flow features such as strong streamline curvature, vortices, and recirculation [27]; for the latter, the Shear-Stress Transport (SST) was selected, because it is reliable across a broader range of flow types [28].

Two distinct definitions for the hydraulic diameter, appearing in the Reynolds number and friction factor, were introduced. By taking a cross-section between two rows of brazed points as reference, it can be approximated as a rectangular surface, allowing for a simplified expression of the hydraulic diameter:

$$D_h = \frac{4A}{\Gamma} \approx 2h \tag{3}$$

where A is the area and Γ the wetted perimeter, assuming $W \gg h$. As discussed in the following sections, the HP wall waviness, along with the brazed regions, causes a continuous and periodic change in A and Γ. Hence, an improved formulation could be applied, as suggested by Piper et al. [29]:

$$\breve{D}_h = \frac{4V_u}{A_{w,u}} \tag{4}$$

with V_u and $A_{w,u}$ that are the volume and the wetted area of the characteristic unit volume, respectively.

2.3. Meshing and Boundary Conditions

As the polyhedral mesh is recognized [30,31] to be the most economical in terms of computational resources, being able to adapt well to complex shapes and produce a cell count approximately one quarter that of the tetrahedral mesh, all the HPs domains were discretized with this type of grid.

For instance, a picture of the central region mesh of S2 on a mid-plane is provided in Figure 6. The mesh was generated using Ansys Fluent Meshing 22 R2.

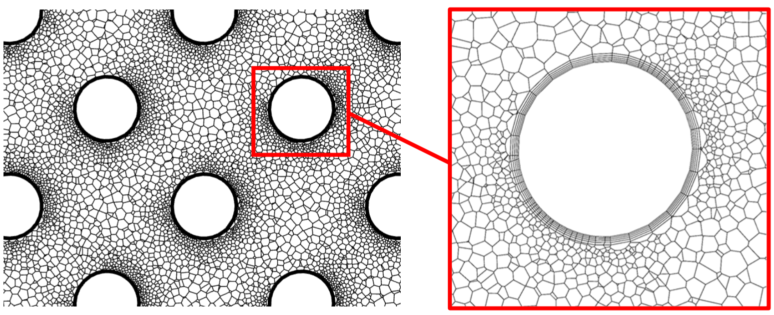

Figure 6. Mesh on the mid-plane and detail of the boundary layer discretization for sample S2.

Prismatic cells were generated for the boundary layers with a uniform method that sets a fixed first layer height, chosen to achieve a near-wall $y^+ \approx 1$, remembering that the following:

$$y^+ = \frac{\rho y u_\tau}{\mu} \tag{5}$$

with $u_\tau = \sqrt{\tau_w/\rho}$. The requirement is commonly recommended when employing the EWT [25] to adequately capture the viscous sub-layer in cases like transitional flows, separations, and heat transfer.

Flow rates measured by a flowmeter were used to set a mass-inlet along with a pressure-outlet boundary at the vessel ends, specifying the hydraulic diameter and a standard value of 5% turbulence intensity at the entrance and a no-slip condition at the walls. Gravity was accounted for.

The SIMPLE algorithm was implemented, with the PRESTO! scheme for pressure and second-order upwind spatial discretization for momentum, turbulent kinetic energy, and dissipation rate.

2.4. Sensitivity Analysis

Several preliminary investigations were conducted to assess the influence of various parameters on the results.

From a geometrical perspective, the primary unknown parameter is the channel height D, which is determined by the placement of the HP surfaces during the domain generation. In practice, it is a result of the entire production process, spanning from initial assembly to the furnace exit, where the brazing material foil undergoes melting.

For the first two matrix samples, a series of calculations was performed with the $k - \varepsilon$ realizable EWT turbulence model for specific Reynolds numbers, varying D, as shown in Figure 7.

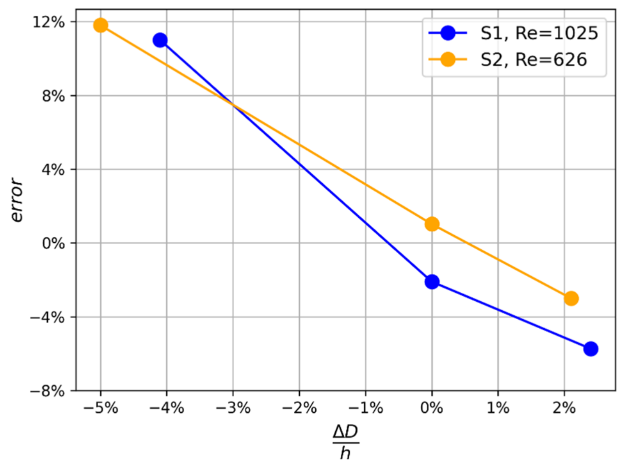

Figure 7. Dependence of numerical results on channel height for S1 and S2 matrices.

On the horizontal axis, the variation ΔD is presented relative to the reference that is $D_0 = 2h$, with h being the nominal height of the dimples of the pressing-dieCAD models. The value of D corresponds to the set distance for the HPs, measured from the top to the bottom points of the dimples. On the vertical axis, the error, defined as the relative difference between the calculated ΔP and experimental ΔP_{exp} pressure drops, is reported.

As observed, D significantly affects ΔP, as expected due to its relationship with the hydraulic diameter. The condition $\Delta P = \Delta P_{exp}$ lies within a narrow range around $D = D_0$.

Taking these errors into account, and with the possibility to ensure a reliable, repeatable approach, all the geometries were therefore created with $D = 2h$.

On the other hand, the effects on ΔP of the matrix were due to the modifications of the brazed-feature diameters by $\pm 10\%$ were negligible, fully covering the measured deviations. Nevertheless, for whole channels, this was not completely true for those near the ports, where higher velocities are experienced and maximum variations of up to $\pm 2\%$ were noted.

To maintain consistency, and considering that such changes can typically arise during the manufacturing process, the brazed joints were modeled with a nearly constant thickness.

A mesh sensitivity analysis was carried out to identify an appropriate element size, as presented for the entire channel of S1 in Figure 8, with the cell count expressed in millions. The focus on this sample is due to the fact that, along with S2, it represents a small-to-medium size BPHE in terms of plate area and capacity, ranging approximately from 20 to 300 kW. Therefore, a limit on the number of cells is necessary to enable calculations for larger devices while preventing unsustainable computational costs. An accuracy improvement of approximately 0.5% was obtained by doubling the cell count from 13.5 to 27 million, which is regarded as too high in light of the long-term perspective of conducting CHT simulations.

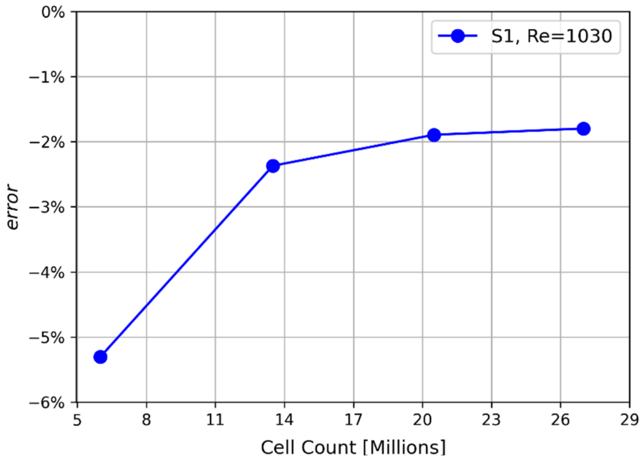

Figure 8. Dependence of numerical results on mesh density for S1 whole plate.

Therefore, the settings used for generating the grid of S1 were chosen and scaled to the other geometries.

Finally, varying the number of prismatic layers between 5 and 10 generally produced an increase in ΔP of less than 1%. Larger values could not be achieved because of failures in volume mesh creation, which occurred where the walls are in close proximity and elements tend to collapse. That minimal impact is believed to be caused by continuous boundary-layer separations, as will be explained in the next section.

3. Results and Discussion

In Table 2, the simulation results for the matrices are listed, comparing the $k-\varepsilon$ realizable with EWT and $k-\omega$ SST schemes. This initial part of the analysis was primarily useful for comprehending the effects of the parameters discussed in Section 2.4, as well as for selecting the appropriate turbulence model.

The $k-\omega$ mostly provided an overestimation of pressure drop, which increases alongside the mass flow rate. With the $k-\varepsilon$, lower ΔP values were observed, along with smaller errors that remained nearly constant at higher Reynolds numbers.

This differing behavior was also detected in the work of Mocnik et al. [13], who attributed it to the so-called "dead zone" that forms behind the brazing points. They suggested that the effect is due to the larger volume of the region predicted when employing the $k-\omega$ model. Looking at these locations, as the flow passes around the obstacles, a wake develops and evolves into a complex structure due to the expanding cross-sectional area downstream. This is illustrated in Figure 9a.

Table 2. Pressure drops results for matrices.

Sample	*Re*	*Error* [%] $k-\varepsilon$	*Error* [%] $k-\omega$
S1	514	−5.4	−3.7
	1025	−2.1	7.2
	1275	−2.0	9.1
S2	466	−2.5	6.4
	626	1.0	7.6
	1046	1.1	9.9
S3	545	−2.2	2.5
	706	−2.0	6.7
	1132	−3.0	11.0

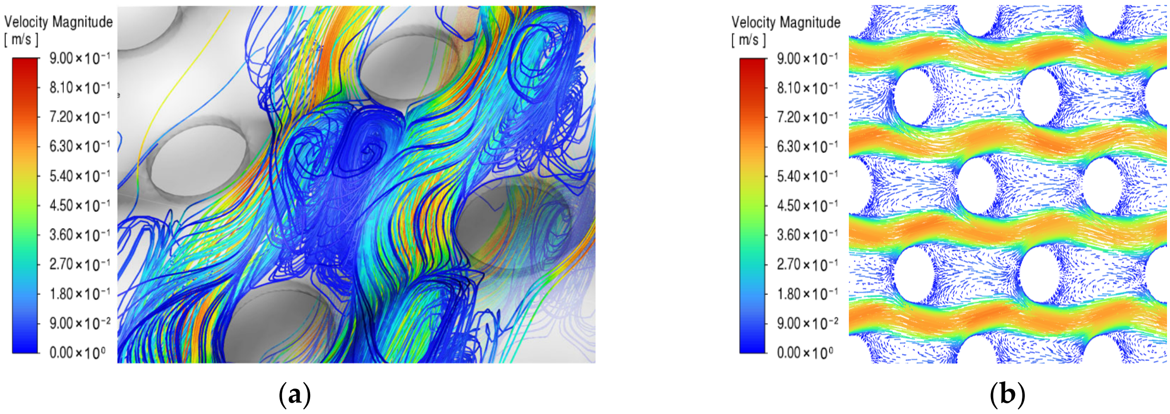

Figure 9. Flow field: (**a**) streamlines passing around the brazed point; (**b**) flow pattern on the mid-plane.

Some fluid particles exhibit a helical upward movement as they fill the channel, while others merge with the mainstream flow between the rows of the brazed points, as depicted in Figure 9b. This pattern is intentional and characterizes the current technology, distinguishing it from the flow in herringbone PHEs, because it features fewer three-dimensional wavy paths having higher velocities magnitude.

A clearer comparison of the results from the two turbulence approaches is achieved by introducing a quantity that more meaningfully represents the losses within a channel, the total pressure P_0, namely the sum of the static and dynamic components.

Figure 10 shows P_0 relative to its maximum value $P_{0,max}$, extracted as a function of the width position w, scaled by the pitch, on a channel cross-section located midway between two consecutive rows of brazed points, for sample S1. The peaks are associated with the preferential flow paths illustrated in Figure 9b, while the minima correspond to the wake cores.

In these regions, the dissipation predicted by $k-\omega$ is higher and remains significant further downstream from the brazed points, unlike the $k-\varepsilon$, which determines a more pronounced tendency toward pressure uniformity, as indicated by the local valleys at the top of the chart.

The greater accuracy provided by the $k-\varepsilon$ realizable with EWT model, along with its ability to align with matrix experimental trends and enable more stable calculations in terms of residuals, led to the decision to use this method for analyzing the entire channels.

Figure 11 presents these calculation results which align with those derived from the matrices, as the HP sample with the lowest profile height (S2) again exhibits positive errors, suggesting a slight overestimation of ΔP.

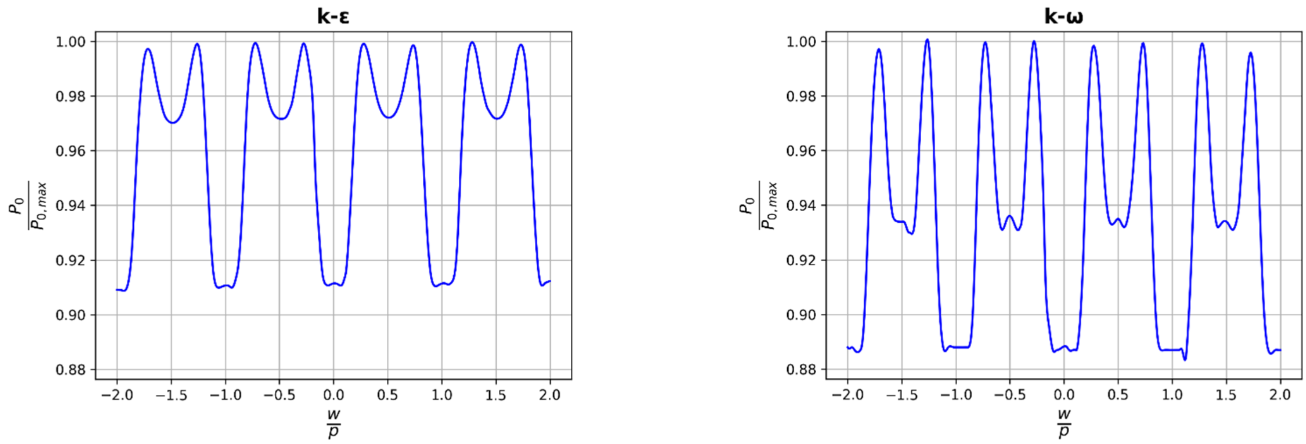

(**a**) (**b**)

Figure 10. Comparison of total pressure trends along the S1 channel width, resulting from (**a**) the $k-\varepsilon$ model and (**b**) the $k-\omega$ model.

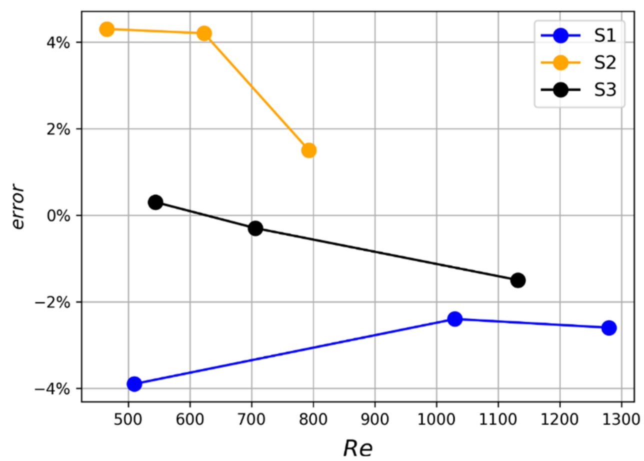

Figure 11. Pressure drops results for the entire channels.

The satisfactory agreement with the experiments confirms the effectiveness of the pre-processing choices, which were based on reproducing the plate geometry using a validated forming procedure and evaluating the impact of various parameters through sensitivity analysis. The global percentage range error is within ±4.4%, with absolute differences below 1 kPa and experimental pressure drops up to 50 kPa; as reported in [13], the measurement uncertainty was 1%.

Further investigation revealed another notable feature. Figure 12 shows a contour of the wall shear stress τ_w, which is generally defined as follows:

$$\tau_w = \mu \left(\frac{\partial v}{\partial y} \right)_{y=0} \tag{6}$$

where v is the velocity tangential to the wall and y the normal direction. Thus τ_w is the force-per-unit area acting on the surface due to friction and serves as an indicator of a boundary-layer separation when it approaches zero.

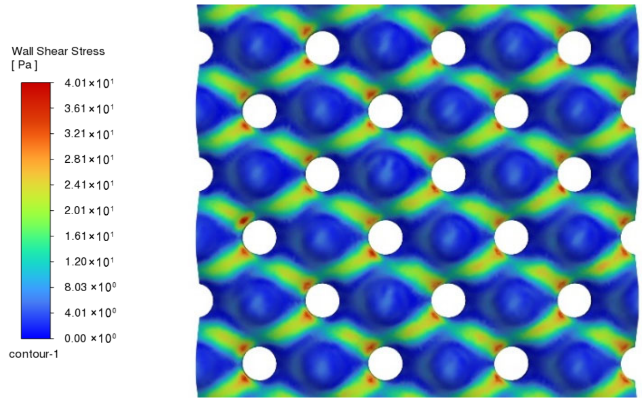

Figure 12. Wall shear stress contour for sample S1, with fluid flowing from left to right.

Higher values of τ_w are observed where the flow accelerates, driven by both the reduction in passage area and the convergence of streamlines near the front surface of the brazed points. On the contrary, downstream, a distinct "V" shape in blue indicates potential flow separation; this occurs as particles encounter a sudden expansion due to the increasing channel height, which reaches its maximum for $D = 2h$. Understanding the distribution of τ_w can be useful for gaining a preliminary insight into the expected heat flux behavior, as the two are connected by the Reynolds analogy [32]. Future simulations incorporating heat transfer will be necessary to demonstrate the actual existence of the mentioned relationship.

Pressure Drops and Friction Factor Analysis

Leveraging the detailed information from the CFD data, an additional investigation was conducted to explore potential enhancements to correlations of the friction factor f, thereby deriving a predictive expression suited to the studied BPHE technology.

For the matrix models, Figure 13 presents a comparison between two sets of f lines, derived from CFD simulations applying the distinct definitions of the hydraulic diameter described in Section 2.2, with the coefficient f calculated from the Darcy–Weisbach equation:

$$f = 2\Delta P \frac{D_h}{L} \frac{1}{\rho U^2} \tag{7}$$

where the characteristic velocity U was determined based on the same cross-section employed in the derivation of Equation (3).

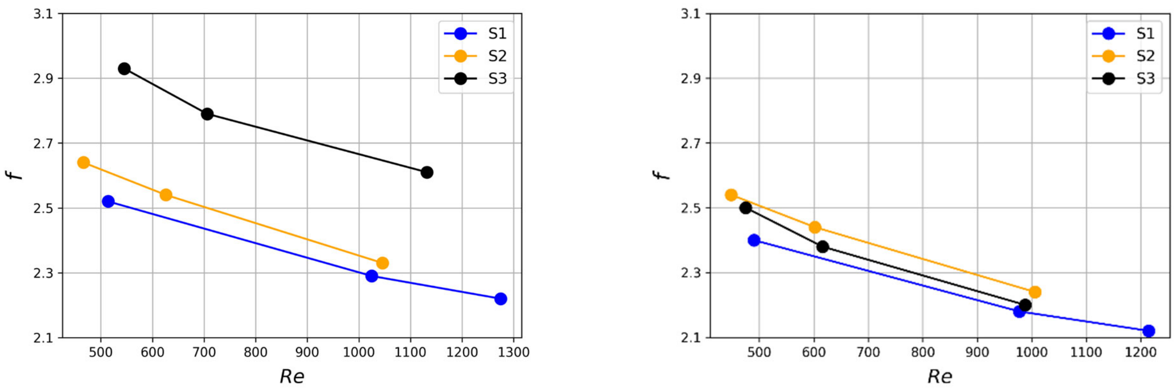

(**a**) (**b**)

Figure 13. Comparison of friction factor trends as a function of Reynolds number, with hydraulic diameter defined by (**a**) Equation (3) and (**b**) Equation (4).

Figure 13b refers to the formula in Equation (4) and shows lower deviations, alongside a greater consistency, suggesting an effective characterization of the hydraulic diameter attributed to its ability to capture the spatial variation of the A/Γ ratio.

The primary challenge in using Equation (4) lies in the need to extract V_u and $A_{w,u}$, which are difficult to predict accurately without relying on 3D geometry, a method used in generating the friction factor data in Figure 13. To create a tool capable of estimating $\breve{D}_h$ without depending on CAD models, the HP unit surface could be approximated as the product of cosine waves:

$$Z = \frac{1}{2}h\left[cos\left(\frac{2\pi}{p}x\right)cos\left(\frac{2\pi}{p}y\right) + 1\right] \tag{8}$$

The plot of Z function is generically illustrated in Figure 14.

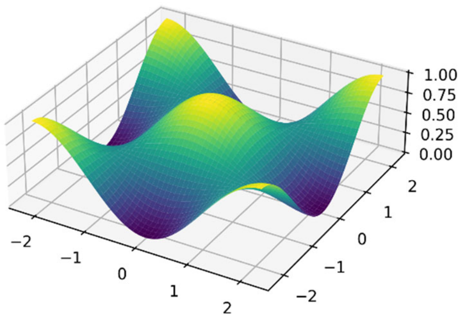

Figure 14. Approximation of the heat plate unit surface using Equation (8).

Due to the symmetry of the plate, the corresponding unit volume is obtained by mirroring Z across the longitudinal plane, therefore V_u is calculated as follows:

$$V_u = 2\iint_{-\frac{p}{2}}^{\frac{p}{2}} Z\, dxdy \tag{9}$$

The infinitesimal area of a surface $Z(x,y)$ in space is expressed as $\sqrt{1 + (\partial Z/\partial x)^2 + (\partial Z/\partial y)^2}\, dxdy$; hence, for function Z:

$$A_{w,u} = 2\iint_{-\frac{p}{2}}^{\frac{p}{2}} \sqrt{1 + \left(\frac{\pi h}{p}\right)^2 B} dxdy \tag{10}$$

with

$$B = (sin(ax)cos(ay))^2 + (sin(ay)cos(ax))^2 \tag{11}$$

and $a = 2\pi/p$.

The calculation of both V_u and $A_{w,u}$ through Equations (9) and (10) was performed using the Gauss–Kronrod quadrature formulae [33]. To achieve higher accuracy, $A_{w,u}$ should be adjusted by subtracting the area relative to the brazed points, whose impact on V_u is negligible due to their minimal thickness; since their measured diameters across the selected geometries are similar, an averaged value was adopted.

Table 3 shows the comparison between the predicted $\breve{D}_h$ values and those obtained from the 3D models.

The relatively small errors highlight the potential of the aforementioned approach to be integrated into a more comprehensive description of the friction factor as a function of the Reynolds number. Nevertheless, extending it to a broader range of geometries and dimple sizes will require the development of a formulation accounting for the variation in brazed points, which future research must focus on.

Table 3. Comparison of hydraulic diameter values.

Sample	CAD $\breve{D}_h/\breve{D}_h^*$	Prediction $\breve{D}_h/\breve{D}_h^*$	*Error* [%]
S1	1.21	1.19	−2
S2	0.82	0.82	1
S3	1	1.03	3

When considering the full plate pressure drops, a greater discrepancy in the f coefficients is observed. This is presumed to arise from the effects of the HP outer regions, which are not fully included in the area-averaged velocity definition.

Generally speaking, and as confirmed by CFD data, a channel can be virtually divided into two main zones, as shown in Figure 15a: a central region (C), where the flow is predominantly aligned along the port-to-port distance, and distribution areas (DAs), where it begins to deviate as it approaches or exits the ports. Near the latter zones, the reduction in the actual passage leads to an increase in velocity magnitude, as illustrated by the contour plot for sample S1 in Figure 15b.

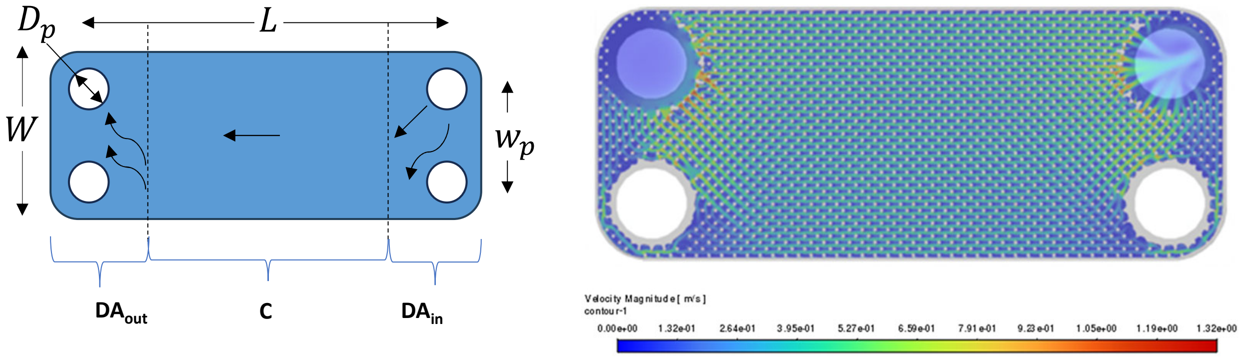

(**a**) (**b**)

Figure 15. Channel regions: (**a**) schematic representation; (**b**) velocity contour for sample S1.

Therefore, in the proximity of inlet and outlet, the pressure trend differs from that observed in the middle part. This becomes evident when studying the gradient $\Delta P/\Delta x$, with x being the longitudinal coordinate measured from the HP center: for instance, a plot of this quantity, averaged over the cross-sectional areas and scaled relative to the value measured at $x = 0$ (denoted as $\Delta P_{mid}/\Delta x$), is depicted for sample S1 in Figure 16, at different Reynolds numbers.

With an almost constant $\Delta P/\Delta x$ in the central region, pressure drops linearly, experiencing a significant increase, which is practically symmetric, where the flow direction changes, before reducing again at the ports. A similar pattern can be extracted by comparing the velocity components along the width, as they grow near the outer zones.

Varying the Reynolds number, the situation remains consistent, as the curves are nearly overlapped, leading to an identical estimation of the distribution areas' extent; this was based on a threshold of a 5% rise in $\Delta P/\Delta x$.

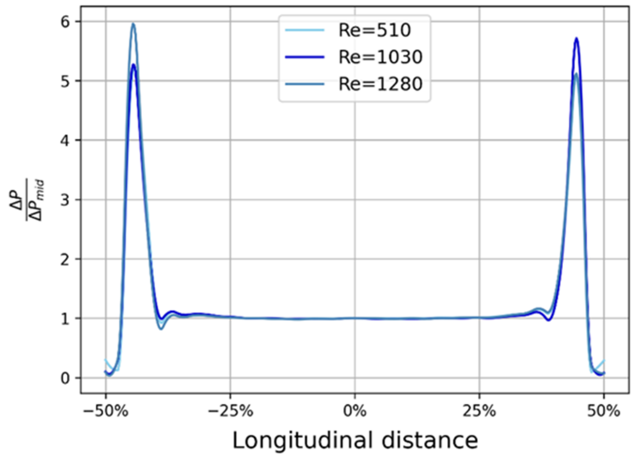

Figure 16. Pressure gradient trends at different Reynolds numbers for sample S1.

Table 4 presents the relative lengths and contributions to the global ΔP for the three examined channel models.

Table 4. Channel regions characteristics.

Sample	Central Region		Distribution Areas	
	Extent [%]	ΔP [%]	Extent [%]	ΔP [%]
S1	59	46	41	54
S2	62	55	38	45
S3	86	95	14	5

The properties of each individual part change across the geometries, explaining their subsequent influence on the friction factor; in particular, the ΔP for sample S3 is primarily determined by the losses along the middle section, as the plate has a high aspect ratio L/W.

To account for these variations and improve the friction factor formulation for a better pressure drops prediction, an analysis has been conducted to incorporate the effects illustrated.

The pressure drop due to the channel passage can be expressed as follows:

$$\Delta P = \Delta P_C + \Delta P_{DA} \tag{12}$$

where ΔP_C is derived by applying Equation (7), with f obtained in both cases from the matrix behavior. Regarding ΔP_{DA}, an analogous equation is employed, with the length and average velocity U_{DA} adjusted to reflect the flow behavior in the external zones. It is assumed to move through a hypothetical stream tube, with one boundary defined by the closed port, which, in conjunction with the open port, directs the flow tangentially to them. This approximation enables the estimation of the reference length L_{DA}, which is used in Equation (7), as well as the longitudinal extent L^*_{DA} of the distribution areas. The concept is depicted in Figure 17.

By introducing the port spacing w_p along the width, L^*_{DA} is written as follows:

$$L^*_{DA} = \frac{W}{2} tan\left(arcsin\left(\frac{D_p}{w_p}\right)\right) \tag{13}$$

with the argument of the arcsine representing the angle between the tangent to the ports and the line connecting their centers.

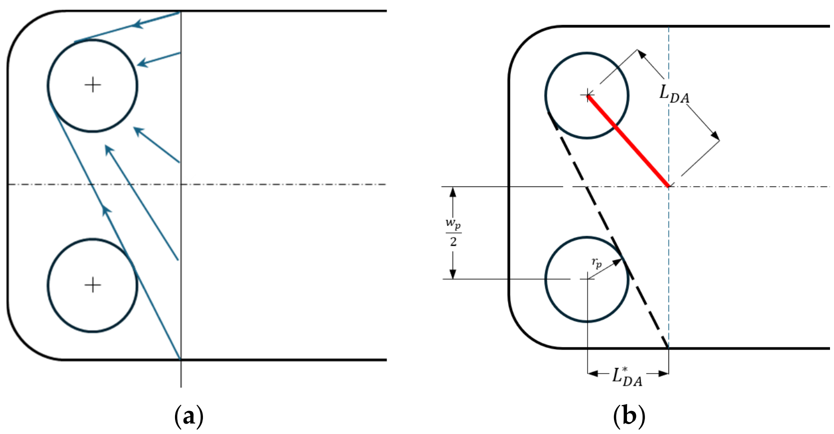

Figure 17. Distribution area: (**a**) stream tube concept; (**b**) main geometrical parameters.

Applying the Pythagoras' theorem:

$$L_{DA} = \sqrt{{L^*_{DA}}^2 + \left(\frac{w_p}{2}\right)^2} \tag{14}$$

The quantity U_{DA} is calculated as the arithmetic average of the magnitude associated with the central region and that corresponding to the minimum passage area at the open port, approximated as $\pi r_p h$ to simplify the procedure. The maximum velocity is thus computed using the continuity equation.

When comparing the results from this approach and CFD data for the contributions of the distribution areas alone, very low absolute errors (<1%) were found for samples S1 and S2, both in terms of their extent and contributions to the global pressure drop, provided that an enlargement factor for the closed port diameter is introduced. The reason lies in the flow being guided by the brazed joint on that side, which is larger than the nominal diameter, thus altering the actual direction of the flow path based on the scheme in Figure 17.

For the mentioned geometries, when adding the ΔP_C component and accounting for the deviations in the friction factor, with the hydraulic diameter as specified in Equation (4), the difference in the pressure drops across the various tested Reynolds numbers remains below $\pm$2.5%.

In contrast, model S3 exhibits higher errors of approximately +7%. This discrepancy arises from a significant portion (~17%) of the fluid mass coming from the central part and navigating through the available passage around the closed port. Indeed, in describing the method and deriving U_{DA}, the initial hypothesis was that the entire flow rate deviates through the imaginary duct constructed along the tangent line. This holds true for S1, where the distance between the brazed wall on the blocked side and the plate edge is minimal. For S2, although the situation is somewhat similar to S3, the HP structure ensures that the passage near the port closely aligns with the one considered in the methodology. Finally, in S3, the flow enters the port in a 360° manner, with higher frontal velocities corresponding to the majority (~83%) of the channel mass flow originating from the middle region.

These results should be viewed as a preliminary attempt to weigh the distribution zones, emphasizing the potential for improving the friction factor correlation by adjusting only the length and velocity, along with refining the specific definition of the hydraulic diameter. Future analyses will be required to develop an even more accurate formulation by incorporating the illustrated flow phenomena near the closed ports.

4. Conclusions

To establish a robust procedure for evaluating the performance of Brazed Plate Heat Exchangers based on dimpled corrugation, a framework combining initial forming simulations and subsequent computational fluid dynamics analyses was developed and validated against experiments on pressure drops, using water as the working fluid. The focus of this preliminary work was to achieve consistent comparisons of quantities associated with flow within the channels while excluding uncertainties arising from external flow effects in the full device. The key findings can be summarized as follows:

- The study successfully extended the analysis of heat plates with a dimple pattern to full-channel configurations, including regions near the ports, addressing a significant gap in existing research.
- The plate distance was found to have a significant impact on the results, with a value of twice the profile height identified as optimal in balancing accuracy and repeatability.
- The $k - \varepsilon$ realizable turbulence model with enhanced wall treatment provided good results in matching both the experimental pressure drops and their trend with the Reynolds number, outperforming the $k - \omega$ SST model in accuracy and stability.
- Leveraging the CFD outcomes, a strategy for estimating pressure drops in different channel regions was proposed as a foundation to significantly reduce reliance on computationally expensive CFD simulations. It includes a revised definition of the hydraulic diameter for capturing the continuous and periodic change in the cross-sectional area and wetted perimeter, which characterizes the dimpled geometry.
- The methodology implemented provides a workflow for enabling further investigations on heat transfer phenomena and optimizing the BPHE design.

Future work should focus on improving the modeling of outer regions to predict flow rate distribution around closed ports and explore conjugate heat transfer CFD simulations. A specific approach will be necessary to overcome the preprocessing limitations in representing the entire object while reliably estimating thermal performance.

Author Contributions: Conceptualization, L.G. and F.G.; methodology, L.G. and F.G.; software, L.G.; validation, L.G.; formal analysis, L.G.; investigation, L.G. and F.G.; resources, F.G.; data curation, L.G.; writing—original draft preparation, L.G.; writing—review and editing, F.G., G.V., U.M., A.M. and L.T.; visualization, L.G.; supervision, F.G., A.M. and L.T.; project administration, F.G. and L.T.; funding acquisition, F.G. and L.T. All authors have read and agreed to the published version of the manuscript.

Funding: This research received no external funding.

Institutional Review Board Statement: Not applicable.

Informed Consent Statement: Not applicable.

Data Availability Statement: Data unavailable due to privacy.

Conflicts of Interest: Author Francesco Giacomelli and Giacomo Villi were employed by the company Danfoss S.r.l. Author Urban Močnik was employed by the company Danfoss Trata d.o.o. The remaining authors declare that the research was conducted in the absence of any commercial or financial relationships that could be construed as a potential conflict of interest.

Abbreviations

The following abbreviations are used in this manuscript:

BPHE	Brazed Plate Heat Exchanger
CFD	Computational Fluid Dynamics
CHT	Conjugate Heat Transfer
EWT	Enhanced Wall Treatment
HP	Heat Plate
PHE	Plate Heat Exchanger
PPHE	Pillow Plate Heat Exchanger
SST	Shear-Stress Transport

Nomenclature

Physical and geometrical quantities:

A	area	m^2
D	diameter, channel height	m
f	Darcy friction factor	
$\vec{g}$	gravity vector	m/s^2
h	profile height	m
k	turbulent kinetic energy	m^2/s^2
L	length	m
Nu	Nusselt number	
P	pressure	Pa
p	pitch	m
r	radius	m
Re	Reynolds number	
U	characteristic velocity	m/s
$\vec{u}$	velocity vector	m/s
u_τ	friction velocity	m/s
V	volume	m^3
v	velocity tangential to the wall	m/s
W	plate width	m
w	width position	m
x	longitudinal distance from plate center	m
y	wall distance	m
y^+	dimensionless wall distance	

Subscripts:

0	total conditions
C	central
DA	distribution areas
exp	experimental
h	hydraulic
max	maximum value
p	port
u	unit volume
w	wall, wetted

Greeks:

Γ	wetted perimeter	m
ε	turbulent dissipation rate	m^2/s^3
μ	dynamic viscosity	Pa s
ρ	density	kg/m^3
τ	shear stress	Pa
ω	specific dissipation rate	s^{-1}

References

1. Kakaç, S.; Liu, H. *Heat Exchangers: Selection, Rating, and Thermal Design*, 2nd ed.; CRC Press: Boca Raton, FL, USA, 2002.
2. Abou Elmaaty, T.M.; Kabeel, A.E.; Mahgoub, M. Corrugated plate heat exchanger review. *Renew. Sustain. Energy Rev.* **2017**, *70*, 852–860. [CrossRef]
3. Zhang, J.; Zhu, X.; Mondejar, M.E.; Haglind, F. A review of heat transfer enhancement techniques in plate heat exchangers. *Renew. Sustain. Energy Rev.* **2019**, *101*, 305–328. [CrossRef]
4. IEA. *The Future of Cooling, Opportunities for Energy-Efficient Air Conditioning*; IEA: Paris, France, 2018. Available online: https://www.iea.org/reports/the-future-of-cooling (accessed on 11 November 2024).
5. Sarraf, K.; Launay, S.; Tadrist, L. Complex 3D-flow analysis and corrugation angle effect in plate heat exchangers. *Int. J. Therm. Sci.* **2015**, *94*, 126–138. [CrossRef]
6. Zhang, Y.; Jiang, C.; Yang, Z.; Zhang, Y.; Bai, B. Numerical study on heat transfer enhancement in capsule-type plate heat exchangers. *Appl. Therm. Eng.* **2016**, *108*, 1237–1242. [CrossRef]
7. Khail, A.A.; Erişen, A. Improvement of Plate Heat Exchanger Performance Using a New Plate Geometry. *Arab. J. Sci. Eng.* **2021**, *46*, 2877–2889. [CrossRef]
8. Khail, A.A.; Erişen, A. Heat transfer and performance enhancement investigation of novel plate heat exchanger. *Therm. Sci. Eng. Prog.* **2022**, *34*, 101368. [CrossRef]
9. Doo, J.H.; Ha, M.Y.; Min, J.K.; Stieger, R.; Rolt, A.; Son, C. An investigation of cross-corrugated heat exchanger primary surfaces for advanced intercooled-cycle aero engines (Part-I: Novel geometry of primary surface). *Int. J. Heat Mass Transf.* **2013**, *55*, 5256–5267. [CrossRef]
10. Doo, J.H.; Ha, M.Y.; Min, J.K.; Stieger, R.; Rolt, A.; Son, C. An investigation of cross-corrugated heat exchanger primary surfaces for advanced intercooled-cycle aero engines (Part-II: Novel geometry of primary surface). *Int. J. Heat Mass Transf.* **2013**, *61*, 138–148. [CrossRef]
11. Gürel, B.; Akkaya, V.R.; Göltaş, M.; Şen, Ç.N.; Güler, O.V.; Koşar, M.İ.; Keçebaş, A. Investigation on flow and heat transfer of compact brazed plate heat exchanger with lung pattern. *Appl. Therm. Eng.* **2020**, *175*, 115309. [CrossRef]
12. Danfoss A/S. Available online: https://www.danfoss.com/en/products/dhs/heat-exchangers/brazed-heat-exchangers/brazed-heat-exchangers/micro-plate-technology/ (accessed on 5 December 2024).
13. Močnik, U.; Blagojevič, B.; Muhič, S. Numerical Analysis with Experimental Validation of Single-Phase Fluid Flow in a Dimple Pattern Heat Exchanger Channel. *Stroj. Vestn. J. Mech. Eng.* **2020**, *66*, 544–553. [CrossRef]
14. Močnik, U.; Čikić, A.; Muhič, S. Numerical and experimental analysis of fluid flow and flow visualization at low Reynolds numbers in a dimple pattern plate heat exchanger. *Energy* **2024**, *288*, 129812. [CrossRef]
15. Močnik, A.; Muhič, S. Experimental and numerical analysis of heat transfer in a dimple pattern heat exchanger channel. *Appl. Therm. Eng.* **2023**, *230*, 120865. [CrossRef]
16. Joybari, M.M.; Selvnes, H.; Sevault, A.; Hafner, A. Potentials and challenges for pillow-plate heat exchangers: State-of-the-art review. *Appl. Therm. Eng.* **2022**, *214*, 118739. [CrossRef]
17. Kumar, S.; Premachandran, B.; Subbarao, P.M.V. Large eddy simulation of single-phase forced convection in pillow plate channel with periodic boundary conditions. *Int. J. Heat Mass Transf.* **2020**, *149*, 119176. [CrossRef]
18. Norouzi, A.; Sodagar-Abardeh, J.; Arabkoohsar, A.; Ismail, K.A.R. Investigating thermo-hydraulic behavior of pillow plate heat exchangers using entropy generation approach. *Chem. Eng. Process. Process Intensif.* **2022**, *174*, 108887. [CrossRef]
19. Piper, M.; Zibart, A.; Kenig, E.Y. New design equations for turbulent forced convection heat transfer and pressure loss in pillow-plate channels. *Int. J. Therm. Sci.* **2017**, *120*, 459–468. [CrossRef]
20. Piper, M.; Zibart, A.; Djakow, E.; Springer, R.; Homberg, W.; Kenig, E.Y. Heat transfer enhancement in pillow-plate heat exchangers with dimpled surfaces: A numerical study. *Appl. Therm. Eng.* **2019**, *153*, 142–146. [CrossRef]
21. Zibart, A.; Kenig, E.Y. Numerical investigation of conjugate heat transfer in a pillow-plate heat exchanger. *Int. J. Heat Mass Transf.* **2021**, *165*, 120567. [CrossRef]
22. ANSYS Inc. *LS_Dyna Theory Manual R14*; ANSYS Inc.: Canonsburg, PA, USA, 2023.
23. Barlat, F.; Brem, J.C.; Yoon, J.W.; Chung, K.; Dick, R.E.; Lege, D.J.; Pourboghrat, F.; Choi, S.-H.; Chu, E. Plane stress yield function for aluminum alloy sheets—Part 1: Theory. *Int. J. Plast.* **2003**, *19*, 1297–1319. [CrossRef]
24. Shah, R.K.; Subbarao, E.C.; Mashelkar, R.A. *Heat Transfer Equipment Design*, 1st ed.; CRC Press: Boca Raton, FL, USA, 1988.
25. ANSYS Inc. *ANSYS Fluent Theory Guide*; ANSYS Inc.: Canonsburg, PA, USA, 2022.
26. Kaplan, S.; Bayramoğlu, K.; Sarikanat, M.; Altay, L. Numerical study on heat transfer and fluid dynamics in plate heat exchangers: Effects of chevron angle and aspect ratio. *J. Therm. Eng.* **2024**, *10*, 638–656. [CrossRef]
27. Shih, T.-H.; Liou, W.W.; Shabbir, A.; Yang, Z.; Zhu, J. A New-Eddy-Viscosity Model for High Reynolds Number Turbulent Flows—Model Development and Validation. *Comput. Fluids* **1995**, *24*, 227–238. [CrossRef]
28. Menter, F.R.; Kuntz, M.; Langtry, R. Ten Years of Experience with the SST Turbulence Model. *Heat Mass Transf.* **2003**, *4*, 625–632.

29. Piper, M.; Olenberg, A.; Tran, J.M.; Kenig, E.Y. Determination of the geometric design parameters of pillow-plate heat exchangers. *Appl. Therm. Eng.* **2015**, *91*, 1168–1175. [CrossRef]
30. Wang, W.; Cao, Y.; Okaze, T. Comparison of hexahedral, tetrahedral and polyhedral cells for reproducing the wind field around an isolated building by LES. *Build. Environ.* **2021**, *195*, 107717. [CrossRef]
31. Peric, M.; Ferguson, S. The Advantage of Polyhedral Meshes. 2005. Available online: http://www.plmmarketplace.com/upload/Temp/The_Advantage_of_polyhedral.pdf (accessed on 22 February 2023).
32. Cengel, Y.A.; Ghajar, A.J. *Heat and Mass Transfer: Fundamentals and Applications*, 5th ed.; Mc Graw Hill: New York, NY, USA, 2015.
33. Calvetti, D.; Golub, G.H.; Gragg, W.B.; Reichel, L. Computation of Gauss–Kronrod rules. *Math. Comput.* **2000**, *69*, 1035–1052. [CrossRef]